

# One-pot synthesis of high-capacity silicon anodes via on-copper growth of a semi-conducting, porous polymer

Michael Bojdys<sup>1</sup>

<sup>1</sup>Humboldt-Universität zu Berlin

January 11, 2022

## Abstract

Silicon-based anodes with lithium ions as charge carriers have the highest predicted theoretical specific capacity of 3579 mA h g<sup>-1</sup> (for Li<sub>15</sub>Si<sub>4</sub>). Contemporary electrodes do not achieve this theoretical value largely because conventional production paradigms rely on the mixing of weakly coordinated components. In this paper, a semi-conductive triazine-based graphdiyne polymer network is grown around silicon nanoparticles directly on the current collector, a copper sheet. The porous, semi-conducting organic framework (i) adheres to the current collector on which it grows via cooperative van der Waals interactions, (ii) acts effectively as conductor for electrical charges and binder of silicon nanoparticles via conjugated, covalent bonds, and (iii) enables selective transport of electrolyte and Li-ions through pores of defined size. The resulting anode shows extraordinarily high capacity at the theoretical limit of fully lithiated silicon. Finally, we combine our anodes in proof-of-concept battery assemblies using a conventional layered Ni-rich oxide cathode.

One-pot synthesis of high-capacity silicon anodes via on-copper growth of a semi-conducting, porous polymer  
Jieyang Huang<sup>[a]</sup>, Andréa Martin<sup>[a]</sup>, Anna Urbanski<sup>[b]</sup>, Ranjit Kulkarni<sup>[a]</sup>, Patrick Amsalem<sup>[c]</sup>, Moritz Exner<sup>[a]</sup>, Johannes Müller<sup>[c]</sup>, David Burmeister<sup>[a]</sup>, Norbert Koch<sup>[c],[d]</sup>, Torsten Brezesinski<sup>[e]</sup>, Nicola Pinna<sup>[a]</sup>, Petra Uhlmann<sup>[b]</sup>, Michael J. Bojdys<sup>\*[a],[f]</sup>

[a] Dr. J. Huang, Dr. A. Martin, Dr. R. Kulkarni, M. Exner, D. Burmeister, Prof. Dr. N. Pinna, Prof. Dr. M. J. Bojdys Institut für Chemie and IRIS Adlershof Humboldt-Universität zu Berlin Brook-Taylor-Str. 2, 12489 Berlin, Germany E-mail: m.j.bojdys.02@cantab.net

[b] Dr. A. Urbanski, Prof. Dr. P. Uhlmann Leibniz-Institut für Polymerforschung Dresden (IPF) e. V Institut für Physikalische Chemie and Physik der Polymere 01069 Dresden, Germany

[c] Dr. P. Amsalem, J. Müller, Prof. Dr. N. Koch Institut für Physik and IRIS Adlershof Humboldt-Universität zu Berlin Brook-Taylor-Str. 2, 12489 Berlin, Germany

[d] Prof. Dr. N. Koch Helmholtz-Zentrum Berlin GmbH Albert-Einstein-Str. 15, 12489 Berlin

[e] Dr. T. Brezesinski Institute of Nanotechnology Karlsruhe Institute of Technology (KIT) Hermann-von-Helmholtz Platz 1, 76344 Eggenstein-Leopoldshafen, Germany

[f] Prof. Dr. M. J. Bojdys Department of Chemistry King's College London Britannia House Guy's Campus, 7 Trinity Street, London, SE1 1DB, UK

Supporting information for this article is given via a link at the end of the document.

**Abstract:** Silicon-based anodes with lithium ions as charge carriers have the highest predicted theoretical specific capacity of 3579 mA h g<sup>-1</sup> (for Li<sub>15</sub>Si<sub>4</sub>). Contemporary electrodes do not achieve this theoretical value largely because conventional production paradigms rely on the mixing of weakly coordinated components.

In this paper, a semi-conductive triazine-based graphdiyne polymer network is grown around silicon nanoparticles directly on the current collector, a copper sheet. The porous, semi-conducting organic framework (i) adheres to the current collector on which it grows via cooperative van der Waals interactions, (ii) acts effectively as conductor for electrical charges and binder of silicon nanoparticles via conjugated, covalent bonds, and (iii) enables selective transport of electrolyte and Li-ions through pores of defined size. The resulting anode shows extraordinarily high capacity at the theoretical limit of fully lithiated silicon. Finally, we combine our anodes in proof-of-concept battery assemblies using a conventional layered Ni-rich oxide cathode.

## Introduction

Cheap, high-performance, and safe energy storage solutions are needed to address the increasing demand for portable electronics and the transition to electric mobility. Lithium-ion batteries have replaced conventional secondary battery technology (like nickel-cadmium and nickel-metal hydride batteries) due to their high energy densities and stable capacity retention in the charged state.<sup>1</sup> Lithium metal anodes were quickly replaced by lithium-intercalated graphitic materials in order to avoid the formation of dendrites that resulted in short circuiting of the two electrodes. However, while lithium-graphite intercalates are safer and more stable they have only a tenth of the energy density of lithium metal.<sup>2</sup> Silicon is a good active material for Li-ion anodes because it has a superior theoretical specific capacity of  $3579 \text{ mA h g}^{-1}$  (or  $8340 \text{ mA h cm}^{-3}$ ) for  $\text{Li}_{15}\text{Si}_4$ , and – unlike some transition metals – it is not toxic and abundant. Moreover, its alloying reaction with lithium triggered at  $0.3 \text{ V vs. Li}^+/\text{Li}$ , prevents the formation of lithium around the anode during charging – a detrimental process observed for graphite-based Li-ion batteries known as “lithium plating” – and allows the use of Si electrodes under harsher conditions.<sup>3</sup> The large number of lithium atoms that silicon can store, however, induces large volume changes during charge/discharge cycling ( $>300\%$ ).<sup>3</sup> The mechanical stress induced by these drastic volume changes leads to the pulverization of the silicon active material, loss of contact of the electrode film with the current collector, and loss of overall mechanical integrity of the whole electrode. Repeated cycles of expansion and contraction of silicon expose pristine silicon surfaces and induce the reformation of solid electrolyte interfaces (SEI). This process contributes to the gradual consumption of lithium and electrolyte, and it limits the diffusion of charge carriers through the expanding SEI.<sup>3-7</sup> It is difficult to counter these detrimental mechanical and chemical changes to silicon-based electrodes because conventional methods of electrode assembly rely on the mixing of multiple components that are held together by weak, dispersive forces.

In laboratory settings, some strategies were developed to address the inherent flaws of these multi-component assemblies. For example, shaping silicon into hierarchical, nano-sized, or porous structures buffers some of its dramatic volume expansion during lithiation.<sup>7</sup> On the downside, nanostructured silicon is susceptible to restructuring during battery operation, and its larger specific surface promotes reactions with the electrolyte to form more of SEI. In other approaches silicon particles are encapsulated in a carbonaceous matrix,<sup>8</sup> or they are coated with metal oxides.<sup>9</sup> However, encapsulation of silicon requires supplementary components that do not meaningfully contribute to the capacity of the electrode and might necessitate the addition of agents that enhance electrical conductivity. Such modifications of the active material prior to electrode assembly have proven too time consuming, low yielding and expensive and, hence, none of these methods have found their way into commercial processes to date.

In this work, we present a departure from the current “blend-and-bake” paradigm of electrode manufacture. In a one-pot process, we embed silicon nanoparticles (Si NPs) in a covalently-linked, porous, semi-conducting polymer matrix whose growth is initiated and templated by the current collector (Cu) itself. The covalent bonds of the organic matrix contribute to a superior mechanical and chemical resistance of our electrode films. The overall  $\pi$ -conjugated backbone of the triazine-based graphdiyne (TzG) polymer enables the transport of electrons from the active material to the current collector. Since the polymerization is promoted by the reactive metal surface of the current collector, the resulting polymer/silicon composite (TzG/Si) adheres strongly to it.<sup>10</sup> In summary, the covalent polymer matrix acts at the same time as (i) a strong binder, as (ii) an electrical conductor, and as (iii) a semi-permeable membrane that enables transport of ions and

electrolyte but prevents the migration of homogeneously dispersed silicon nanoparticles even under harsh conditions. This facile method yields silicon-based anodes (TzG/Si@Cu) of superior performance that suffer little mechanical and electrochemical deterioration from the inherent volume expansion of silicon during lithiation-delithiation and that drastically limit the detrimental loss of lithium and electrolyte at the SEI.

## Results and Discussion

Electrodes of TzG/Si@Cu are prepared by dissolving the organic monomer 2,4,6-tris(4-ethynylphenyl)-1,3,5-triazine and dispersing Si NPs in pyridine in a 25%:75% weight ratio, respectively. The reaction mixture is then transferred onto a copper foil (Figure 1a; Supplementary Information Section S1, Scheme S1 and S2). Residual Cu(II) and Cu(I) species on the untreated copper surface initiate the polymerization *via* a Glaser-type oxidative coupling reaction.<sup>11-13</sup> The polymerization is driven to completion and the pyridine is removed by evaporation.<sup>10</sup> <sup>13</sup>C cross-polarization / magic-angle-spinning (CP/MAS) solid-state NMR (Figure 1b) shows the characteristic signals of a triazine-based graphdiyne polymer;<sup>10</sup> the triazine carbon at ~170 ppm and the diyne-bridges at 75-85 ppm. An additional signal seen at ~30 ppm is attributed to O<sub>2</sub>SiMe<sub>2</sub> surface groups originating from the preparation of these commercially available Si NPs. This is corroborated by <sup>29</sup>Si single-pulse-magic-angle-spinning (SP-MAS) solid-state NMR (Figure S1) and Fourier transform infrared (FT-IR) spectra (Figure S2).<sup>14-16</sup> The Raman spectrum of TzG/Si@Cu (Figure 1c) shows stretching bands of diyne C[?]C at 2209 cm<sup>-1</sup>, of triazine C=N at 1411 cm<sup>-1</sup>, of phenyl C=C at 1604 cm<sup>-1</sup>, and of crystalline Si-Si bonds at 518 cm<sup>-1</sup>.<sup>10,17,18</sup>

X-ray photoelectron spectroscopy (XPS) performed on c-axis oriented layers of TzG/Si@Cu show all expected carbon environments in the C 1s region that are observed for the neat TzG polymer (Figure S3a).<sup>10</sup> In addition, Si 2p spectra show the presence of surface silicon oxide, SiO<sub>x</sub> (~34%) and neat silicon (66%) (Figure S3b), compared to as-received Si NPs that contain 21% of SiO<sub>x</sub> and 79% of Si(0) environments (Figure S3d).<sup>19-22</sup> In summary, spectroscopic analysis confirms the formation of a covalent, conjugated, triazine-based polymer network around chemically unchanged Si NPs.

For comparison, we have prepared three different types of electrode systems *via* the same one-pot method described above but with varying compositions to carefully test the effects of individual components: (i) growing a film of TzG on Cu, we obtain TzG@Cu, (ii) growing TzG in the presence of Si NPs we get TzG/Si@Cu (in ratio 25/75 wt%), and (iii) TzG/Si/CB@Cu (in ratio 20/60/20 wt%) is produced by growing TzG around Si NPs and a conventional electronically conductive additive, carbon black (CB) (Supplementary Information Section S1.5).

Scanning electron microscopy (SEM) images reveal the morphology of pristine TzG/Si@Cu electrodes. The material grown on the copper support adopts a porous, sponge-like, and homogeneous morphology as seen top-down (Figure 1e) and from cross-sections of the electrode film (Figure 1f). Cross-sectional SEM imaging at lower magnifications shows films of TzG/Si with a thickness of ~25 μm that adhere well to the Cu substrate with no apparent gaps (Figure S4). More detailed transmission electron microscopy (TEM) energy-filtered mapping on TzG/Si films shows a homogenous distribution of carbon and silicon on the nanometer level (Figure 1g). On the nanoscale, the electrode film consists of Si NPs homogeneously embedded in an organic polymer matrix of TzG. Residual Cu nanoparticles (less than 1 wt%) can be seen within the polymer matrix that stem from the TzG polymerization process (Figure 1h; a comparison of TEM images of TzG@Cu and of pristine Si NPs can be found in Figure S5).<sup>10</sup> Overall, individual Si NPs are enclosed by the conjugated, polymer and held cooperatively as a film on the current collector.

We have shown previously that neat, unmodified triazine-based graphdiyne polymers are narrow band-gap semiconductors ( $E_{g,elec} = 1.84$  eV and conductivity of 1.2 μS cm<sup>-1</sup> at RT) with moderate porosities (N<sub>2</sub> BET surface area of 124 m<sup>2</sup> g<sup>-1</sup> at 77 K).<sup>10,23</sup> Hence, the composite TzG/Si on Cu foil (TzG/Si@Cu) has a promising combination of chemical, electrical, and structural features for electrochemical energy storage applications.

In the following (Supplementary Information Section S2.1), we discuss the electric and electrochemical performance of TzG-based electrodes and the effects of the TzG polymer on the formation of the SEI. For the

three electrode systems TzG/Si@Cu, TzG/Si/CB@Cu, and TzG@Cu (i) we compared the bulk conductivities of the un lithiated, “as-synthesized” electrodes (Figure S6), (ii) we recorded cyclic voltammetry (CV) curves (Figure S7), and (iii) we performed ex-situ XPS measurements probing the electrode surfaces to a depth of approx. 10 nm after a number of de-/lithiation cycles (Figure 2a; Figure S8, S9, S10 and S13; Table S1; details of the XPS spectra fitting method are described in Supplementary Information section S1.7). During the first lithiation of the TzG/Si@Cu electrode, the resulting

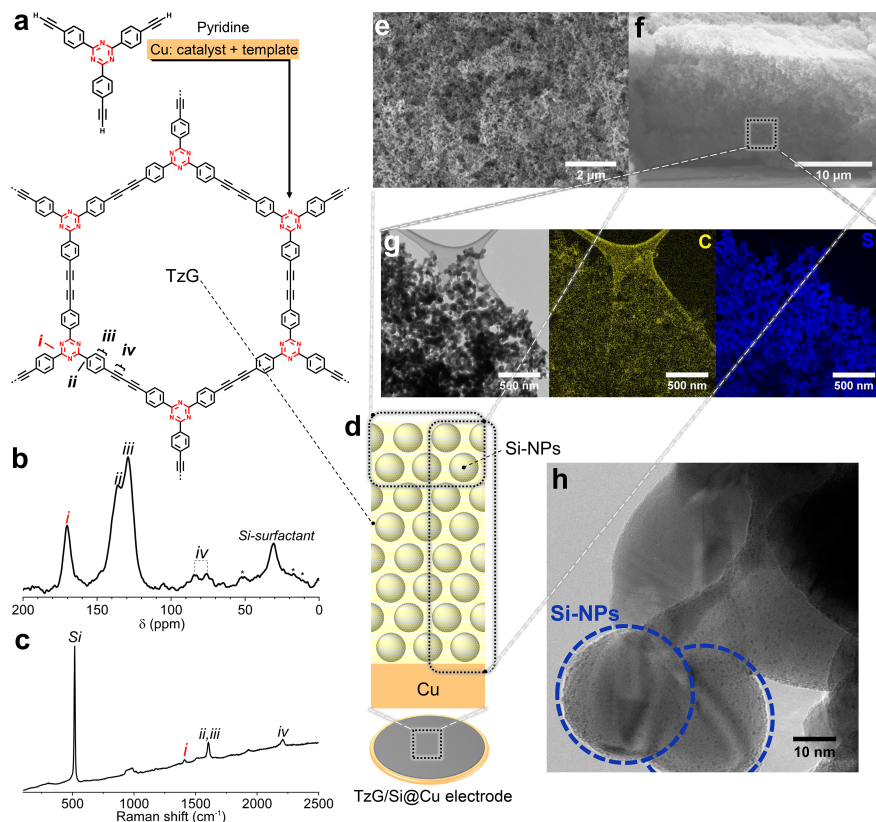


**Figure 1.** Micro- and macroscopic characterization of the chemical make-up of TzG/Si@Cu (TzG/Si = 25/75 wt%) electrodes. **a**, Synthetic pathway for the triazine-based graphdiyne (TzG) polymer. Spectroscopic characterization showing the corresponding **b**,  $^{13}\text{C}$  cross-polarization / magic-angle-spinning (CP/MAS) solid-state NMR spectrum of the TzG/Si polymer composite, and **c**, the Raman spectrum with fluorescence background collected with a 532 nm laser. **d**, Schematic of the TzG/Si@Cu electrode. Scanning electron microscopy (SEM) images showing **e**, the top-view surface morphology and **f**, the cross section morphology of TzG/Si@Cu films. **g**, Low-resolution transmission electron microscopy (TEM) images and energy-filtered mapping images showing the homogenous distribution of carbon and silicon environments, and **h**, high-resolution TEM images showing Si NPs fully enclosed by TzG polymer.

composition of the film presents a content with up to 43.9 mol% of cumulative Li, F, and P elements (Table 1). Furthermore, after the first cycle of lithiation and delithiation, we observe that the initial Si 2p signal of the pristine electrode decreases dramatically in intensity from 40.8 mol% to a value close to zero (Table 1). The fitting of C 1s, F 1s and Li 1s spectra (Figure S10) indicates the formation of the SEI during the first lithiation, resulting in the variations of surface elemental concentration mentioned above. Note though that even after the 100th delithiation event, we detect a signal of Si(0) in the Si 2p region (Figure 2a, iv, Table 1). This finding suggests that SEI formation is completed at an early stage, and that SEI thickness does not increase dramatically throughout cycling.<sup>24,25</sup> XPS data from the Si 2p region of TzG/Si@Cu electrodes

cycled at C/8 (Figure 2a) shows the emergence of new Si 2p peaks corresponding to  $\text{Li}_x\text{Si}$ ,  $\text{SiO}_x\text{F}_y$ , and  $\text{Li}_x\text{SiO}_y$  after the first-cycle lithiation.<sup>19-22</sup> The presence of  $\text{SiO}_x\text{F}_y$  presumably results from the non-faradic reaction between the remaining  $\text{LiPF}_6$  and the  $\text{SiO}_x$  on the surface of the Si NPs, during the opening of the cell for ex-situ measurement.<sup>19</sup> The environments of  $\text{Li}_x\text{Si}$  and  $\text{Li}_x\text{SiO}_y$  originate from the electrochemical alloying reaction of silicon and  $\text{SiO}_x$  with the lithium ions in the electrolyte, as further corroborated by emerging signals in the F 1s and Li 1s regions (Figure S10b and S10c).<sup>20,22</sup> Pristine and delithiated samples of TzG/Si@Cu all show peaks corresponding to Si(0) and  $\text{SiO}_x$ , indicating a fully reversible de-/lithiation process.

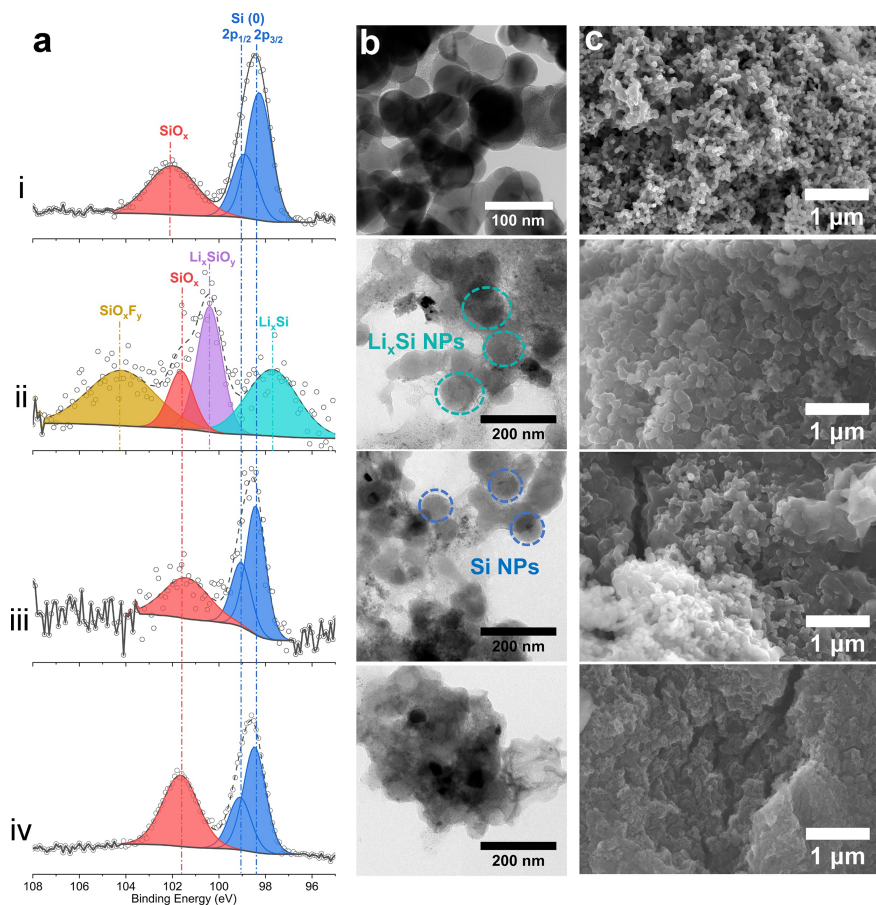


**Figure 2.** Characterization of TzG/Si@Cu electrodes using **a**, X-ray photoelectron spectroscopy (XPS) data from the Si 2p region, **b**, transmission electron microscopy (TEM), and **c**, scanning electron microscopy (SEM). Data is presented for TzG/Si@Cu electrodes in the pristine state (i), after the first lithiation (ii), after the first delithiation (iii) and after the 100<sup>th</sup> delithiation (iv). Cycling was performed using constant current mode at C/8 within a voltage range of 0.01-1.2 V vs.  $\text{Li}^+/\text{Li}$ .

Ex-situ TEM and SEM imaging of TzG/Si@Cu electrodes at different cycling stages (Figure 2b and c) reveal that prior to cycling, the TzG polymer acts as a binder that joins Si NPs into a porous TzG/Si composite (i). After the first lithiation, individual particles of increased size can be discerned that correspond to lithiated and volumetrically expanded domains of  $\text{Li}_x\text{Si}$ , all embedded in a fabric of polymer and SEI (ii). After the first delithiation, the size of the spherical Si domains decreases (iii), and after the 100<sup>th</sup>-cycle delithiation, all that can be said is that the TzG/Si composite shows no discernible large cracks or deformations (iv) (Figure S11 and S12).

A comprehensive discussion of these findings is presented in Supplementary Information section S2.2. For now, we conclude that: (i) the alloying reaction between lithium and Si NPs takes place unhindered, hence, the TzG polymer matrix allows lithium to diffuse, (ii) the conductivity enhancing additive in TzG/Si/CB@Cu has no positive effect on the performance of TzG-based electrodes, hence, the initial, modest conductivity of undoped TzG is no impediment for its use in electrodes; and (iii) the TzG polymer does not participate in the detrimental depletion of lithium or electrolyte on its own, and SEI formation occurs exclusively in the presence of Si NPs. It is particularly surprising that TzG-based electrodes perform as well as they do, given their

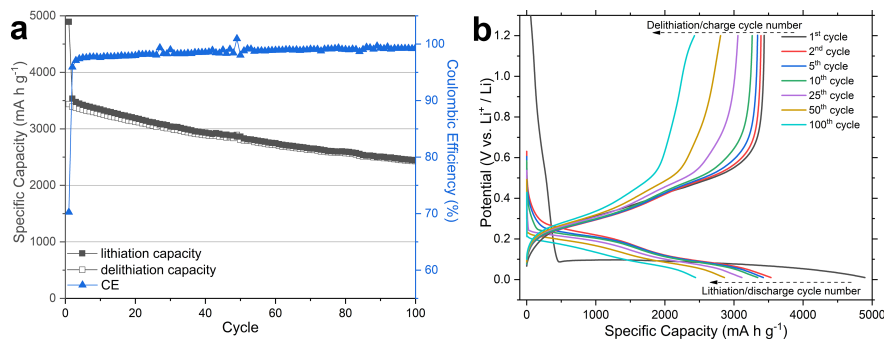


**Figure 3.** Half-cell performance data of the TzG/Si@Cu electrodes. Galvanostatic charge-discharge cycling with potential limitation (GCPL) uses constant current mode at C/8 within a voltage range of 0.01-1.2 V vs. Li<sup>+</sup>/Li. **a**, Specific capacities normalized to Si mass and Coulombic efficiencies (CE) vs. cycle number. **b**, Potential vs. specific capacity curves for consecutive de-/lithiation cycles.

low conductivity in the pristine, unlithiated state. While an in-depth study of the electrical conductivity of lithiated TzG/Si@Cu is out of the scope of this work, XPS results for TzG@Cu suggest that the first lithiation cycle leads to n-doping of the TzG polymer by N 1s signal shifting to higher binding energy (Figure S8),<sup>26-28</sup> analogous to lithiated graphite,<sup>29,30</sup> and, hence, to an increase of its conductivity above and beyond the effect achieved by the conducting additive in TzG/Si/CB@Cu.

We subjected the TzG/Si@Cu electrode to de-/lithiation cycling at C/8 in a half-cell set-up recording specific capacity (Figure 3). In the first lithiation cycle, we observe the formation of the SEI at a comparatively low CE value of ~70%, meaning that the surface of Si NPs is readily accessible for lithium and for the electrolyte *via* the pore channels of the TzG polymer. Similar Coulombic efficiencies have been reported for nanosized silicon particles with a large external surface area. Microsized silicon particles with a smaller ratio of exposed surfaces show higher initial CE values but suffer from limited lithiation capacities and poor cycling performance.<sup>31</sup> In the third cycle, the CE rises above 97% and steadily improves up to 99.5% which means that SEI formation is completed early on. The specific capacity observed during the first lithiation exceeds the theoretical value for Li<sub>15</sub>Si<sub>4</sub> (3579 mA h g<sup>-1</sup>) due to the formation of the SEI.<sup>32-34</sup> Starting with the second cycle, no excess capacity is recorded and, hence, the newly formed SEI does not contribute to the measured discharge capacity. The recorded specific lithiation capacity in the second cycle is ~3500 mA h g<sup>-1</sup>, and it remains at a record high in subsequent cycles (*e.g.* ~3450 mA h g<sup>-1</sup> in the fifth cycle). In comparison, the TzG/Si/CB@Cu electrode prepared together with carbon black does not perform better than the additive-free electrode (Figure S14). Taking the specific lithiation capacity in the second cycle as a baseline, TzG/Si@Cu retains 81.0% of its specific capacity after 50 cycles (2862 mA h g<sup>-1</sup>) and 69.1% after 100 cycles (2443 mA h g<sup>-1</sup>). Conversions of these values to areal and volumetric capacities can be found in Figure S15.

For comparison, we prepared two electrodes using conventional binders and CB additive, PVdF/Si/CB@Cu and PAA/Si/CB@Cu (Figure S16).<sup>21,35</sup> These conventional formulations allow a total Si mass loading of up to 60% without compromising the performance of the electrode, compared to 75% of Si in the TzG/Si@Cu

system. Overall, the specific capacity of TzG/Si@Cu

**Table 1.** Relative molar concentrations of elements as determined by peak integration using X-ray photoelectron spectroscopy (XPS) data recorded at 1486.6 eV for TzG/Si@Cu electrodes at various stages of de-/lithiation cycled at a constant current of 0.32 mA cm<sup>-2</sup> (i.e. C/8 for the capacity of Si, within 0.01-1.2 V vs. Li<sup>+</sup>/Li). (Calculated based on XPS C 1s, Si 2p N 1s, O 1s, Li 1s, F 1s and P 2p spectra).

Sample	Stage during cycling	C (%)	Si (%)	N (%)	O (%)	Li (%)	F (%)	P (%)
TzG/Si@Cu	pristine	17.8	40.8	2.17	39.3	0.00	0.00	0.00
TzG/Si@Cu	1st lithiation	23.0	1.90	0.65	28.2	28.1	15.8	2.36
TzG/Si@Cu	1st delithiation	29.4	1.71	0.16	27.3	22.4	17.8	1.24
TzG/Si@Cu	100th delithiation	44.5	0.84	0.00	32.0	15.9	6.31	0.44

anodes exceeds that of the best-performing multi-component systems with and without conductivity-enhancing additives that are reported to date (Table S3).<sup>36-45</sup> We tuned mass-loading of TzG/Si@Cu electrodes that lead to similar excellent performance (Supplementary information Table S2, Section S2.6, Figure S17-S19). For example, we were able to increase the Si mass-loading of the electrode beyond 1 mg cm<sup>-2</sup> by a two rounds of polymerisation on top of a TzG/Si@Cu electrode in the presence of small quantities of Cu(OAc)<sub>2</sub> as an additional source of Cu(II) species (Supplementary Information Section S1.6, Table S2). The obtained electrodes show a stable cycling performance and comparably high capacities as electrodes obtained in a one-step growth process (Figure S19).

TzG is a thermally stable polymer with a decomposition onset above 400 °C under air.<sup>10</sup> Hence, we tested the performance of the TzG/Si@Cu half-cell after a heat treatment of 80 °C for 6 h, above temperatures experienced by Li-ion batteries in some industrial and military settings. The overall performance of the TzG/Si@Cu half-cell after the thermal-stress test remains at ~3000 mA h g<sup>-1</sup> in the second cycle comparable to the performance of untreated electrodes. The difference in overall capacity and in capacity retention can be attributed to partial decomposition of LiPF<sub>6</sub> during the extended heat treatment (Figure S20). As a proof of concept, we assembled a full cell using TzG/Si@Cu as the anode and the commercially available standard NCM811 as the cathode (Figure S21 and S22). The NCM811 cathode was selected over three commercial options (NCM532, NCM622, and NCA) as the one with the highest specific capacity and most stable cycling performance. We believe that full-cell assemblies with better coulombic efficiencies can be achieved using cathodes that (i) match the high capacity of our anode better, and (ii) have similar diffusion kinetics.

## Conclusion

We present here a one-pot synthetic protocol that yields high-performance silicon anodes within one hour of reaction time. These anodes consist of silicon nanoparticles that are fully encapsulated by a semi-conducting, porous triazine-based graphdiyne (TzG) polymer that grows directly on the Cu current collector. Cu foil plays three roles in this paradigm-changing method of anode fabrication: it acts (i) as a source of Cu species for a Glaser-type oxidative coupling polymerization, (ii) as templating substrate for the polymer film, and (iii) as the current collector of the electrode. The porous, semi-conducting TzG polymer acts (i) as a strong, flexible binder that envelops Si NPs with a matrix of covalent bonds that can sustain the dramatic volume changes of silicon in repeated de-/lithiation cycles and prevents detrimental abrasion and reformation of the solid electrolyte interface, (ii) as a facilitator of charge transport along its  $\pi$ -conjugated polymer backbone, and (iii) as a medium for mass transport of lithium ions and electrolyte through its microporous channels. The resulting anodes achieve stable electrochemical cycling performance and an extraordinarily high capacity close to the theoretical limit of electrochemical storage using silicon. The reported process uses raw materials and methods common in industrial electrode manufacture and can be transferred and scaled up with ease. Half-cell electrode assemblies in the off-state retain key performance parameters even after thermal stress, and full-cell cycling tests using commercial cathodes demonstrate the viability of this technology in commercial applications.

## Acknowledgements

We thank Dr. Martin Dračinský for solid-state NMR measurements, Dr. Petr Formánek for TEM imaging and mapping, Prof. Dr. Jürgen P. Rabe for access to Raman spectroscopy. J.H. thanks Dr. Mathias Trunk for providing monomer materials, Weimiao Wang for Raman spectra discussion and analysis. M.J.B. thanks the European Research Council (ERC) for funding under the Starting Grant Scheme (BEGMAT-678462) and the Proof of Concept Grant Scheme (LiAnMat-957534).

**Keywords:** graphdiyne \* glaser-coupling \* Li-ion battery \* silicon anode \* one-pot

1 Schmich, R., Wagner, R., Horpel, G., Placke, T. & Winter, M. Performance and cost of materials for lithium-based rechargeable automotive batteries. *Nat. Energy* **3** , 267 (2018).

2 Xu, J. *et al.* Recent progress in graphite intercalation compounds for rechargeable metal (Li, Na, K, Al)-ion batteries. *Adv. Sci.* **4** , 1700146 (2017).

3 Kwon, T.-w., Choi, J. W. & Coskun, A. The emerging era of supramolecular polymeric binders in silicon anodes. *Chem. Soc. Rev.* **47** , 2145-2164 (2018).

4 Eshetu, G. G. & Figgemeier, E. Confronting the challenges of next-generation silicon anode-based lithium-ion batteries: role of designer electrolyte additives and polymeric binders. *ChemSusChem* **12** , 2515-2539 (2019).

5 Cao, P., Pan, Y., Gao, S., Sun, F. & Yang, H. Polymer binders constructed via dynamic non-covalent bonds for high-capacity silicon-based anodes. *Chem. Eur. J.* **25** , 10976-10994 (2019).

6 Li, P. *et al.* Recent progress on silicon-based anode materials for practical lithium-ion battery applications. *Energy Storage Mater.* **15** , 422-446 (2018).

7 Feng, K. *et al.* Silicon-based anodes for lithium-ion batteries: from fundamentals to practical applications. *Small* **14** , 1702737 (2018).

8 Liu, N. *et al.* A yolk-shell design for stabilized and scalable Li-ion battery alloy anodes. *Nano Lett.* **12** , 3315-3321 (2012).

9 Nguyen, H. T. *et al.* Alumina-coated silicon-based nanowire arrays for high quality Li-ion battery anodes. *J. Mater. Chem.* **22** , 24618-24626 (2012).

10 Schwarz, D. *et al.* Twinned growth of metal-free, triazine-based photocatalyst films as mixed-dimensional (2D/3D) van der Waals heterostructures. *Adv. Mater.* **29** , 1703399 (2017).

11 Mohwald, H., Bliznyuk, V. & Kirstein, S. Structure, energy and charge transport in two-dimensional crystals of cyanine dyes. *Synth. Met.* **61** , 91-96 (1993).

12 Li, Y., Xu, L., Liu, H. & Li, Y. Graphdiyne and graphyne: from theoretical predictions to practical construction. *Chem. Soc. Rev.* **43** , 2572-2586 (2014).

13 Vyas, V. S. *et al.* A tunable azine covalent organic framework platform for visible light-induced hydrogen generation. *Nat. Commun.* **6** , 1-9 (2015).

14 Uhlig, F. & Marsmann, H. C. <sup>29</sup>Si NMR some practical aspects. *Gelest Catalog* , 208-222 (2008).

15 Park, C.-M. *et al.* Characterizations and electrochemical behaviors of disproportionated SiO and its composite for rechargeable Li-ion batteries. *J. Mater. Chem.* **20** , 4854-4860 (2010).

16 Mijatovic, J., Binder, W. H. & Gruber, H. Characterization of surface modified silica nanoparticles by <sup>29</sup>Si solid state NMR spectroscopy. *Microchim. Acta* **133** , 175-181 (2000).

17 Larkin, P., Makowski, M. & Colthup, N. The form of the normal modes of s-triazine: infrared and Raman spectral analysis and ab initio force field calculations. *Spectrochim. Acta - A: Mol. Biomol. Spectrosc.* **55** , 1011-1020 (1999).

- 18 Li, H. *et al.* The crystal structural evolution of nano-Si anode caused by lithium insertion and extraction at room temperature. *Solid State Ion.* **135** , 181-191 (2000).
- 19 Philippe, B. *et al.* Role of the LiPF<sub>6</sub> salt for the long-term stability of silicon electrodes in Li-ion batteries—A photoelectron spectroscopy study. *Chem. Mater.* **25** , 394-404 (2013).
- 20 Radvanyi, E., De Vito, E., Porcher, W. & Larbi, S. J. S. An XPS/AES comparative study of the surface behaviour of nano-silicon anodes for Li-ion batteries. *J. Anal. At. Spectrom.* **29** , 1120-1131 (2014).
- 21 Nguyen, C. C., Yoon, T., Seo, D. M., Guduru, P. & Lucht, B. L. Systematic investigation of binders for silicon anodes: interactions of binder with silicon particles and electrolytes and effects of binders on solid electrolyte interphase formation. *ACS Appl. Mater. Interfaces* **8** , 12211-12220 (2016).
- 22 Ferraresi, G., Czornomaz, L., Villeveille, C., Novak, P. & El Kazzi, M. Elucidating the surface reactions of an amorphous Si thin film as a model electrode for Li-ion batteries. *ACS Appl. Mater. Interfaces* **8** , 29791-29798 (2016).
- 23 Schwarz, D. *et al.* Tuning the porosity and photocatalytic performance of triazine-based graphdiyne polymers through polymorphism. *ChemSusChem* **12** , 194-199 (2019).
- 24 Xu, J. Investigation of the critical role of polymeric binders for silicon negative electrodes in lithium-ion batteries. *Theses and Dissertations—Chemical and Materials Engineering.* **68** , [https://uknowledge.uky.edu/cme\\_etds/68](https://uknowledge.uky.edu/cme_etds/68) (2016).
- 25 Koo, B. *et al.* A highly cross-linked polymeric binder for high-performance silicon negative electrodes in lithium ion batteries. *Angew. Chem. Int. Ed.* **51** , 8762-8767 (2012).
- 26 Putri, L. K. *et al.* Engineering nanoscale p–n junction via the synergetic dual-doping of p-type boron-doped graphene hybridized with n-type oxygen-doped carbon nitride for enhanced photocatalytic hydrogen evolution. *J. Mater. Chem. A* **6** , 3181-3194 (2018).
- 27 Sakaushi, K. *et al.* An energy storage principle using bipolar porous polymeric frameworks. *Angew. Chem. Int. Ed.* **51** , 7850-7854 (2012).
- 28 Sezen, H. & Suzer, S. Communication: Enhancement of dopant dependent x-ray photoelectron spectroscopy peak shifts of Si by surface photovoltage. *J. Chem. Phys.* **14** , 141102 (2011).
- 29 Wertheim, G., Van Attekum, P. T. M. & Basu, S. Electronic structure of lithium graphite. *Solid State Commun.* **33** , 1127-1130 (1980).
- 30 Andersson, A. M., Henningson, A., Siegbahn, H., Jansson, U. & Edström, K. Electrochemically lithiated graphite characterised by photoelectron spectroscopy. *J. Power Sources* **119** , 522-527 (2003).
- 31 Ren, W.-F. *et al.* Improving the electrochemical property of silicon anodes through hydrogen-bonding cross-linked thiourea-based polymeric binders. *ACS Appl. Mater. Interfaces* **13** , 639–649 (2021).
- 32 Obrovac, M. & Christensen, L. Structural changes in silicon anodes during lithium insertion/extraction. *Electrochem. Solid-State Lett.* **7** , A93-A96 (2004).
- 33 Kovalenko, I. *et al.* A major constituent of brown algae for use in high-capacity Li-ion batteries. *Science* **334** , 75-79 (2011).
- 34 Urbanski, A. *et al.* An efficient two-polymer binder for high-performance silicon nanoparticle-based lithium-ion batteries: a systematic case study with commercial polyacrylic acid and polyvinyl butyral polymers. *J. Electrochem. Soc.* **166** , A5275-A5286 (2019).
- 35 Karkar, Z., Guyomard, D., Roué, L. & Lestriez, B. A comparative study of polyacrylic acid (PAA) and carboxymethyl cellulose (CMC) binders for Si-based electrodes. *Electrochim. Acta* **258** , 453-466 (2017).

- 36 Chen, Z. *et al.* High-area-capacity silicon electrodes with low-cost silicon particles based on spatial control of self-healing binder. *Adv. Energy Mater.* **5** , 1401826 (2015).
- 37 Choi, S., Kwon, T.-w., Coskun, A. & Choi, J. W. Highly elastic binders integrating polyrotaxanes for silicon microparticle anodes in lithium ion batteries. *Science* **357** , 279-283 (2017).
- 38 Higgins, T. M. *et al.* A commercial conducting polymer as both binder and conductive additive for silicon nanoparticle-based lithium-ion battery negative Electrodes. *ACS Nano* **10** , 3702-3713 (2016).
- 39 Jeong, Y. K. *et al.* Millipede-inspired structural design principle for high performance polysaccharide binders in silicon anodes. *Energy Environ. Sci.* **8** , 1224-1230 (2015).
- 40 Liu, G. *et al.* Polymers with tailored electronic structure for high capacity lithium battery electrodes. *Adv. Mater.* **23** , 4679-4683 (2011).
- 41 Song, J. *et al.* Interpenetrated gel polymer binder for high-performance silicon anodes in lithium-ion batteries. *Adv. Funct. Mater.* **24** , 5904-5910 (2014).
- 42 Wang, C. *et al.* Self-healing chemistry enables the stable operation of silicon microparticle anodes for high-energy lithium-ion batteries. *Nat. Chem.* **5** , 1042 (2013).
- 43 Wu, H. *et al.* Stable Li-ion battery anodes by in-situ polymerization of conducting hydrogel to conformally coat silicon nanoparticles. *Nat. Commun.* **4** , 1943 (2013).
- 44 Zeng, W. *et al.* Enhanced ion conductivity in conducting polymer binder for high-performance silicon anodes in advanced lithium-ion batteries. *Adv. Energy Mater.* **8** , 1702314 (2018).
- 45 Zhang, G. *et al.* A quadruple-hydrogen-bonded supramolecular binder for high-performance silicon anodes in lithium-ion batteries. *Small* **14** , 1801189 (2018).